

## RESEARCH ARTICLE

10.1002/2016JC012149

## Ocean mixing beneath Pine Island Glacier ice shelf, West Antarctica

Satoshi Kimura<sup>1,2</sup>, Adrian Jenkins<sup>1</sup>, Pierre Dutrieux<sup>3</sup>, Alexander Forryan<sup>4</sup>, Alberto C. Naveira Garabato<sup>4</sup>, and Yvonne Firing<sup>5</sup>

## Key Points:

- We present the turbulent kinetic energy and thermal variance dissipation rates beneath an ice shelf for the first time
- The highest thermal variance dissipation rate is found near the ice/ocean interface
- The highest turbulent kinetic energy dissipation rate is found near the grounding line

## Correspondence to:

S. Kimura,  
skimura04@gmail.com

## Citation:

Kimura, S., A. Jenkins, P. Dutrieux, A. Forryan, A. C. Naveira Garabato, and Y. Firing (2016), Ocean mixing beneath Pine Island Glacier ice shelf, West Antarctica, *J. Geophys. Res. Oceans*, 121, 8496–8510, doi:10.1002/2016JC012149.

Received 12 JUL 2016

Accepted 6 NOV 2016

Accepted article online 11 NOV 2016

Published online 7 DEC 2016

<sup>1</sup>British Antarctic Survey, Cambridge, UK, <sup>2</sup>Nansen Environmental and Remote Sensing Center and Bjerknes Centre for Climate Research, Bergen, Norway, <sup>3</sup>Lamont-Doherty Earth Observatory, Columbia University, Palisades, New York, USA, <sup>4</sup>University of Southampton, Southampton, UK, <sup>5</sup>National Oceanography Centre, Southampton, UK

**Abstract** Ice shelves around Antarctica are vulnerable to an increase in ocean-driven melting, with the melt rate depending on ocean temperature and the strength of flow inside the ice-shelf cavities. We present measurements of velocity, temperature, salinity, turbulent kinetic energy dissipation rate, and thermal variance dissipation rate beneath Pine Island Glacier ice shelf, West Antarctica. These measurements were obtained by CTD, ADCP, and turbulence sensors mounted on an Autonomous Underwater Vehicle (AUV). The highest turbulent kinetic energy dissipation rate is found near the grounding line. The thermal variance dissipation rate increases closer to the ice-shelf base, with a maximum value found  $\sim 0.5$  m away from the ice. The measurements of turbulent kinetic energy dissipation rate near the ice are used to estimate basal melting of the ice shelf. The dissipation-rate-based melt rate estimates is sensitive to the stability correction parameter in the linear approximation of universal function of the Monin-Obukhov similarity theory for stratified boundary layers. We argue that our estimates of basal melting from dissipation rates are within a range of previous estimates of basal melting.

## 1. Introduction

Many of the rapidly thinning ice shelves are located in the Amundsen Sea embayment in Antarctica [Pritchard *et al.*, 2009; Rignot *et al.*, 2013; Paolo *et al.*, 2015]. In particular, Pine Island Glacier (PIG) ice shelf has been highlighted as a major drainage pathway of the West Antarctic Ice Sheet [Shepherd *et al.*, 2001], which contains enough water to raise the global eustatic sea level by  $\sim 3$  m [Bamber *et al.*, 2009]. Over the past few decades, the ice shelf has gone through dramatic acceleration in the flow speed and thinning [Joughin *et al.*, 2003; Shepherd *et al.*, 2001]. PIG is grounded on a bed that deepens inland of the grounding line, and there are no topographic barriers to halt retreat once the grounding line reaches the sloping bed [Rignot *et al.*, 2014]. Ice sheet models predict that an irreversible retreat is already underway on this ice shelf, largely in response to the high ice-shelf thinning rate [Joughin *et al.*, 2014; Favier *et al.*, 2014].

The leading explanation of the ice-shelf thinning is unsteady ocean-driven melting [Payne *et al.*, 2004; Shepherd *et al.*, 2004]. Unsteady ocean-driven melting reduces the restraints on the flow of grounded ice sheets upstream [Schoof, 2007; Gudmundsson, 2013] and structurally weakens the ice shelves by forming basal channels in the undersides of ice shelves [Alley *et al.*, 2016], leading to the inland migration of the grounding line. The retreat of the grounding line will increase the discharge of the ice from the land to the ocean, leading to an increase in ice sheets' contribution to the sea level rise.

The origin of unsteady ocean-driven melting lies in the heat content of the surrounding ocean. The Amundsen Sea Embayment is renowned for the presence of almost undiluted Circumpolar Deep Water (CDW) beneath the pycnocline [Jacobs *et al.*, 1996; Jenkins *et al.*, 1997; Walker *et al.*, 2007; Jacobs *et al.*, 2011; Assmann *et al.*, 2013; Dutrieux *et al.*, 2014a]. This CDW is a few degrees above the in situ freezing point and is able to flow beneath the ice shelf, and so drive basal melting [Jenkins *et al.*, 2010].

Sampling oceanic conditions beneath the ice shelf is necessary to advance our understanding of the connection between the basal melting and oceanic forcing. However, observations are limited by the difficulty in gaining access through the ice shelf itself. Some oceanic measurements have been made beneath PIG ice shelf by either drilling a borehole through the ice shelf [Stanton *et al.*, 2013] or sending an Autonomous

Underwater Vehicle (AUV) beneath the ice shelf [Jenkins *et al.*, 2010], both of which require a heavy logistical operation.

Measurements through boreholes beneath PIG ice shelf revealed a stratified ice-shelf-ocean boundary layer [Stanton *et al.*, 2013]. They found that the flow within the boundary layer is dominated by the melt-generated buoyancy acting on the sloping base of the ice shelf. While measurements through boreholes can provide long term record, the spatial coverage is limited by the locations of the boreholes. An AUV survey has a large spatial coverage, but with a short temporal length due to battery life (often up to a few days). AUV and airborne radar surveys have characterized general aspects of the ice-shelf morphology and ocean cavity bathymetry of PIG [Jenkins *et al.*, 2010; Vaughan *et al.*, 2012; Dutrieux *et al.*, 2014b]. A bathymetric survey by the AUV revealed a ridge oriented perpendicular to the ice flow and indicated that the ice was formerly grounded on top of the ridge [Jenkins *et al.*, 2010]. Retreat of the grounding line has since resulted in the formation of a large ocean cavity behind the ridge. This transverse ridge separates the PIG cavity into two gyres and interaction of these gyres modulates the ocean water properties near the grounding line [De Rydt *et al.*, 2014; Dutrieux *et al.*, 2014a].

The ridge presents an obstruction for the CDW intrusion toward the grounding line, and the ocean mixing processes in the gap above the ridge crest can dictate how quickly the replenishment of CDW occurs at the grounding line. Near the ice, the strength of mixing dictates the transport of heat and salt through the ice-shelf-ocean boundary layer, controlling the basal melting which in turn changes the seaward flow of the grounded ice upstream. Identifying mixing hot spots inside the ice-shelf cavity thus is of interest to both glaciologists and oceanographers.

We present microstructure measurements taken by the AUV, Autosub3, beneath PIG ice shelf. We begin with our procedure for processing microstructure measurements from the AUV in section 2. Sections 3 and 4 describe an overview of ocean mixing along and across the ice flow, respectively. The measurements near the ice and their implications for PIG ice-shelf melting are discussed in section 5, and conclusions are summarized in section 6.

## 2. Measurements and Methods

A self-contained instrument package for turbulence microstructure measurement, Rockland Scientific MicroRider, was mounted in the nose of the AUV. The AUV was launched in February 2014 from the *RRS James Clark Ross* as a part of the U.K.'s Ice Sheet Stability programme (iSTAR). The AUV operated with a mean speed of  $1.4 \text{ m s}^{-1}$  and completed two missions totaling 92 h and covering 460 km of track beneath PIG ice shelf (Figure 1). The speed of the AUV is used to convert the unit of measurements made in time rate of change (Hz) into the spatial gradient (cycle per meter, cpm). The first mission (track A) took a series of profiles along the ice flow over a transverse ridge in the sea floor, located approximately 20 km from the calving front. The second mission was launched 2 days after the first mission and followed two separate tracks, B and C (Figure 1). Track B was aligned in the direction of the ice flow, whereas track C was a transverse direction. Tracks B and C sampled oceanographic conditions near the grounding line: B reached a point approximately 10 km away from the eastern grounding line, and C reached a point 2 km away from the southern parts of the grounding line. The AUV microstructure observations are complemented by shipboard microstructure measurements, which are used to evaluate the quality of the microstructure measurements from the AUV.

### 2.1. Processing of Microstructure Data From the AUV

The turbulent kinetic energy dissipation rate,  $\epsilon$  is the rate at which turbulent kinetic energy is converted into internal energy of fluid (heat) through viscosity. The  $\epsilon$  is estimated from shear microstructure measurements with a sampling frequency of 512 Hz, assuming the isotropic relation  $\epsilon = 7.5\nu\langle w_x'^2 \rangle$ , where  $\nu = 1.83 \times 10^{-6} \text{ m}^2 \text{ s}^{-1}$  is the viscosity of seawater and  $\langle w_x'^2 \rangle$  is the shear variance of the velocity,  $w$ , perpendicular to the AUV path  $x$ . The variance is calculated by integrating the shear spectrum up to a cutoff wave number. The path of the AUV is maintained within  $\pm 20^\circ$  from the horizontal direction to ensure that the shear probe responds linearly to cross-stream velocity fluctuation as described in Osborn and Crawford [1980].

The raw shear signals are contaminated by vibrations of the AUV and acoustic devices for communication with the ship. The accelerometer signals from the MicroRider picked up two periodic spikes of 600 s and 0.5 s. These periodic spikes are removed and zero padded. The remaining signal contamination was

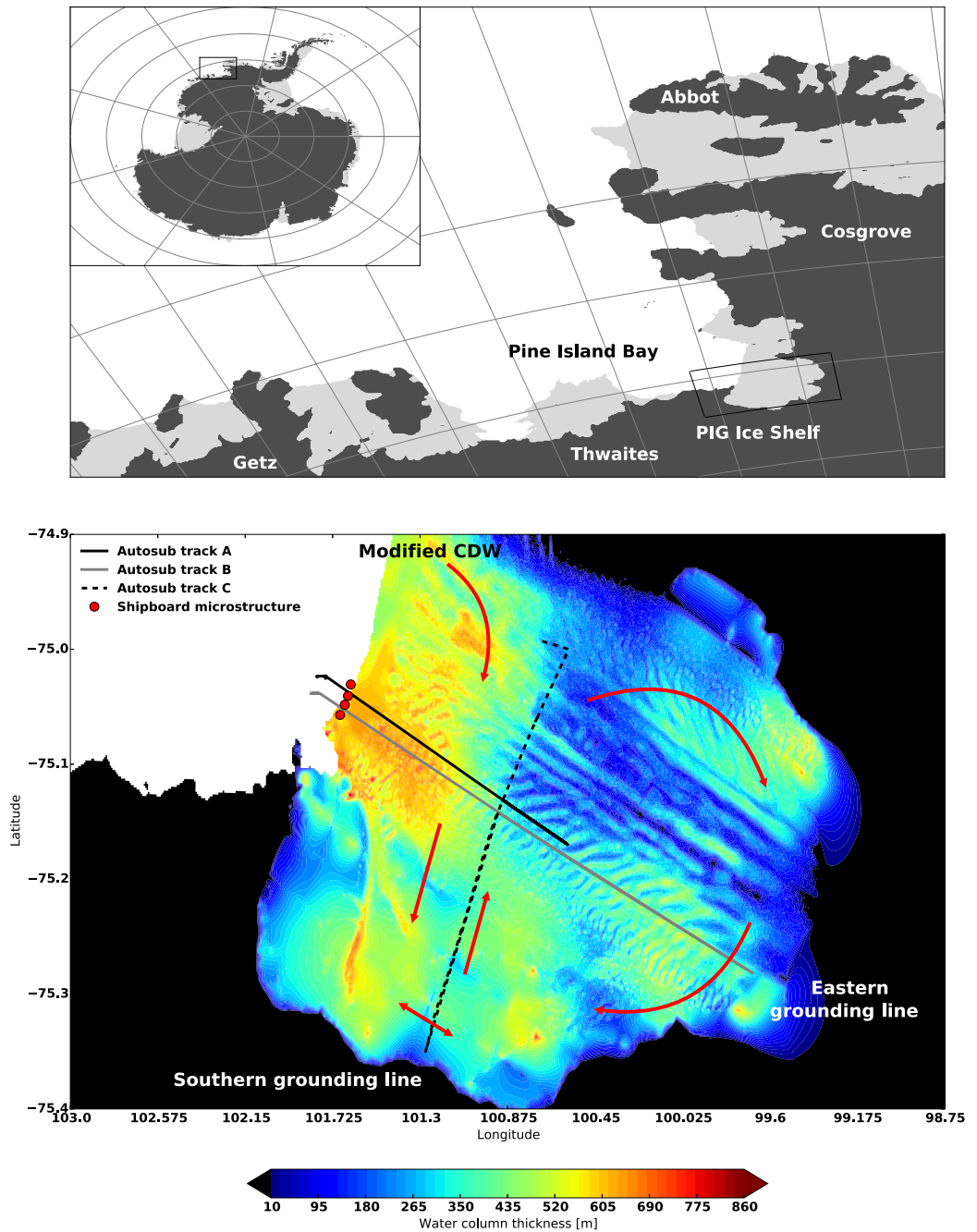


**Figure 1.** Maps showing the Amundsen Sea and Pine Island Bay. Three Autosub mission tracks beneath PIG ice shelf and locations of the shipboard microstructure measurements. The water column thickness beneath the ice shelf is color coded. The water column thickness is defined as the difference between the sea bed depth and ice draft derived from upward looking ADCP mounted on the AUV. Red arrows indicate a schematic representation of CDW inflow into the ice-shelf cavity and its circulation.

removed from the shear power spectra by constructing a filter from the accelerometer signals, following the method outlined in *Levine and Lueck* [1999].

The universal spectra are generated by fitting the variance of the measured shear power spectra for 1 s segments of recorded data between the limits 1–25 cpm for dissipations above  $1 \times 10^{-8} \text{ W kg}^{-1}$  and between 1 and 12 cpm for dissipations below  $1 \times 10^{-8} \text{ W kg}^{-1}$ . Within the integration limits, the observed shear spectra compare well with the universal Nasmyth spectrum (Figure 2). The AUV vibration does not appear to contaminate the shear spectrum in a relatively energetic environment, and the observed shear spectrum

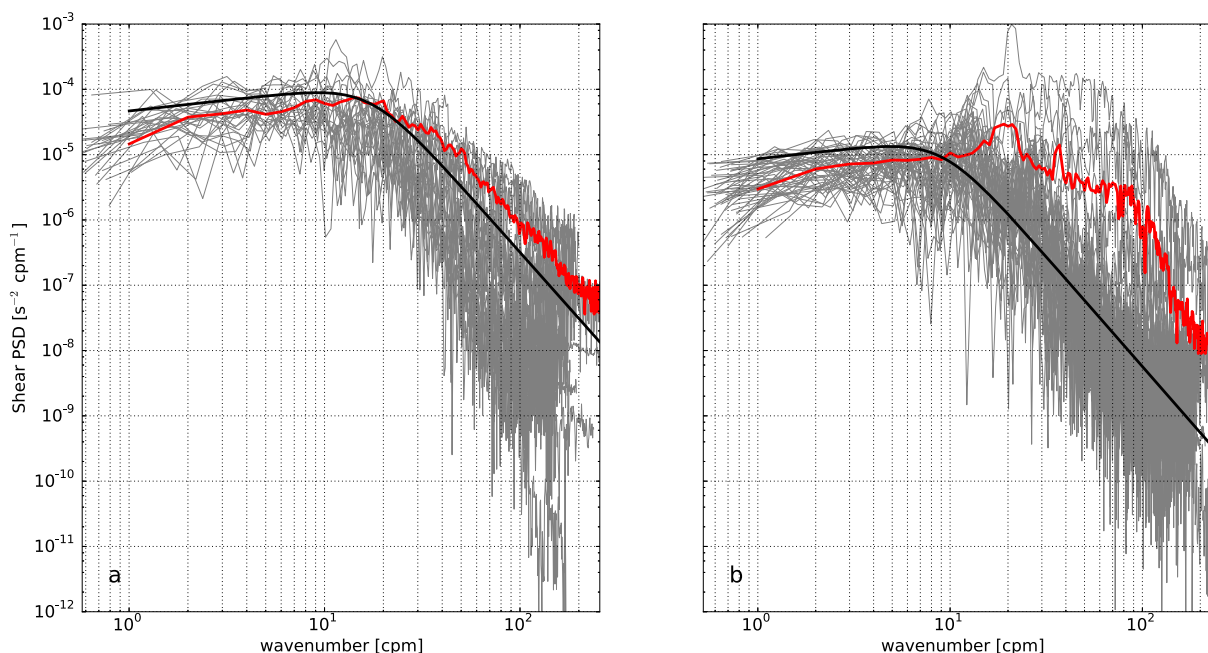


**Figure 2.** Power spectra for (a)  $\epsilon \approx 1.3 \times 10^{-8} \text{ W kg}^{-1}$  (18 spectra) and (b)  $\epsilon \approx 1 \times 10^{-9} \text{ W kg}^{-1}$  (41 spectra). The individual spectra are shown in gray and the mean spectra are shown in red. The dark curves indicate the corresponding Nasmyth universal spectra for each  $\epsilon$ .

is in good agreement with the spectral roll-off of the universal Nasmyth spectrum (Figure 2a). In contrast, the spectral roll-off is not well captured in a less energetic environment, and the contamination from AUV motion appears as a spurious peak between 14 and 22 cpm in the shear spectra (Figure 2b).

When two different water masses are in contact with each other (e.g., glacial meltwater and CDW), thermal anomalies are created. The rate at which the thermal anomalies blend into the background by molecular heat diffusion is the thermal variance dissipation rate,  $\chi_T$ , defined as  $\chi_T = 6\kappa_T((\partial T'/\partial x)^2)$ , where  $\kappa_T = 1.37 \times 10^{-7} \text{ m}^2 \text{ s}^{-1}$  is the molecular diffusivity of heat, and  $\partial T'/\partial x$  is the temperature gradient. The temperature gradient along the path of the AUV,  $x$  is computed from FP07 thermistors mounted on the MicroRider. The thermistor signal is calibrated against on board CTD measurements by fitting to a second-order polynomial. The variance of the thermal gradient is estimated by fitting the Batchelor spectrum [Batchelor, 1959] to the observed spectrum.

The individual estimates of  $\epsilon$  and  $\chi_T$  from 1 s segments are averaged over 20 s windows to obtain more robust estimates of  $\epsilon$  and  $\chi_T$ . These averaged estimates are in good agreement with the shipboard microstructure measurements from the free-falling microstructure instrument, a Rockland Scientific VMP-250 (Figures 3a and 3b). The shipboard microstructure measurements were taken within 4 km of the AUV track a few days prior to the deployment of the AUV. Possible sources of energetic flow at the calving front are the meltwater outflow and the baroclinic shear imposed by the melting ice. The vigorous flow associated with these mechanisms is likely to occur shallower than the ice draft (400 m in PIG ice shelf), and the meltwater outflow is expected at the southern part of the calving front. The AUV track was 450 m or more below the surface to avoid a potential collision with the calving front of the ice shelf, so the comparison with the shipboard data was only possible over a limited depth range. Despite these limiting factors, 82% of  $\epsilon$  and 60% of  $\chi_T$  estimates from the AUV are within the range of shipboard estimates. There appear to be no biases in the estimates; 8% of  $\epsilon$  and 20% of  $\chi_T$  estimates are lower than the shipboard measurements, and 10% of  $\epsilon$  and 20% of  $\chi_T$  estimates are higher than the shipboard measurements. The  $\epsilon$  estimates from the AUV are more consistent with the shipboard measurements than the  $\chi_T$  estimates. This is likely due to the high variability of  $\chi_T$ . The measurements were taken near the thermocline depth, which separates Winter Water (WW) and CDW, and where the glacial meltwater from the cavity interacts with the ambient ocean water, both of which produce strong temperature gradients. The mean  $\epsilon$  from the shipboard and AUV measurements are  $4.8 \times 10^{-10} \text{ W kg}^{-1}$  and  $2.2 \times 10^{-10} \text{ W kg}^{-1}$ , respectively. These values are comparable to the

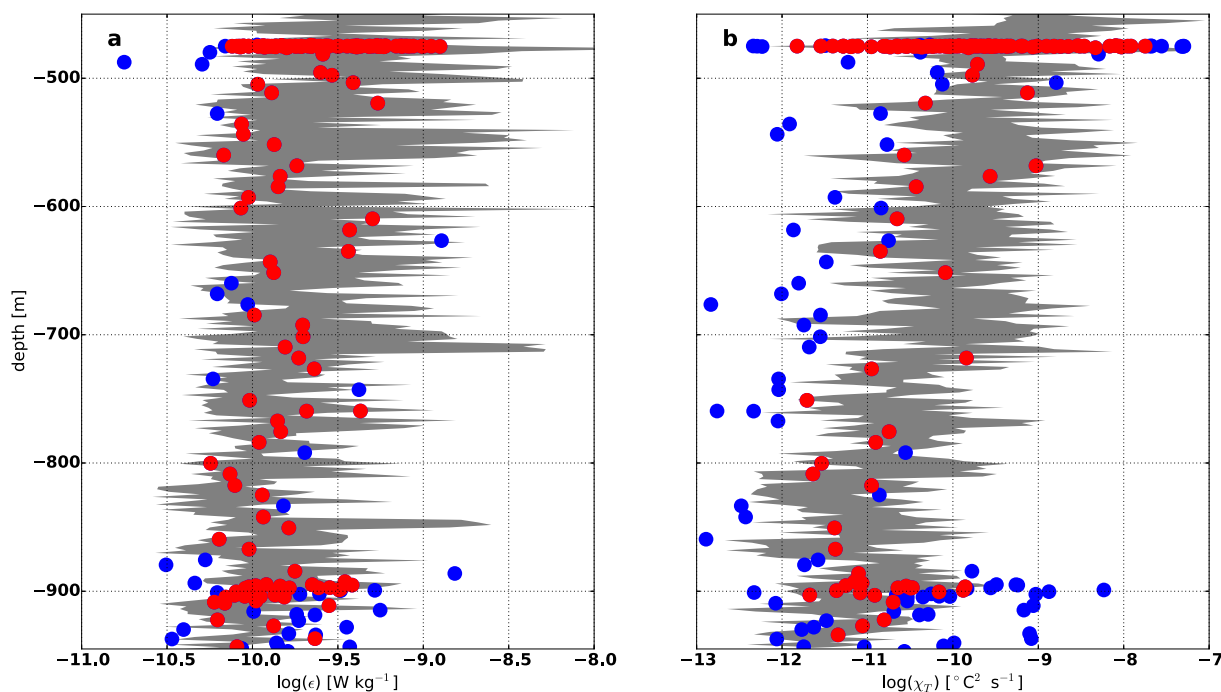


**Figure 3.** Comparison of the shipboard and AUV microstructure measurements (a)  $\epsilon$  and (b)  $\chi_T$ . The shaded region shows the range of  $\epsilon$  and  $\chi_T$  profiles from four shipboard measurements within 4 km of the AUV track. The location of four shipboard measurements is indicated in Figure 1. Red dots indicate the AUV measurements that lie within the shaded region, whereas the measurements outside of the shaded region are color coded in blue. The AUV was sampling along the horizontal direction at the depth of  $-900$  m before entering the ice-shelf cavity and at the depth of  $-480$  m after exiting the cavity, so the measurements outside of the cavity are concentrated at these depths.

background turbulence of the ocean. Both measurements suggest that the depth below the ice draft, slightly north of the southern calving front, in 2014 is not an energetic environment. The fluctuation of  $\epsilon$  is relatively small compared with that of  $\chi_T$ , resulting in better agreement between the noncoincident AUV and shipboard measurements.

### 3. Observations Along the Ice Flow From the Calving Front to the Eastern Grounding Line (Autosub Tracks A and B)

Below the pycnocline (depth  $> 600$  m) inside the cavity is flooded by CDW, but the warmest CDW does not penetrate over the ridge (Figure 4a). At the crest of the ridge, modified CDW is in contact with meltwater-rich cooler and fresher water, increasing the horizontal temperature gradient. The region of high density gradient combined with changes in the water column thickness coincides with the region of high shear motion. The region with the largest values of  $\chi_T$  and  $\epsilon$  ( $\chi_T \sim 10^{-5} \text{ } ^\circ\text{C}^2 \text{ s}^{-1}$  and  $\epsilon \sim 10^{-7} \text{ W kg}^{-1}$ ) is found near the seabed between 35 and 36 km away from the calving front of the ice shelf, where the ridge slopes toward the grounding line (Figures 4b and 4c). These  $\chi_T$  and  $\epsilon$  are several orders of magnitude higher than the average values outside the cavity (Figures 3a and 3b). Both  $\chi_T$  and  $\epsilon$  decrease to the background values away from the ridge and increase again near the eastern grounding line.

The three major water masses in Pine Island Bay are CDW, WW, and meltwater [Jacobs *et al.*, 2011]. Broadly speaking, the water column in Pine Island Bay consists of cool ( $T \sim -1.5 \text{ } ^\circ\text{C}$ ), fresh ( $S < 34.4$  psu) WW over warm ( $T \sim 1 \text{ } ^\circ\text{C}$ ), salty ( $S > 34.6$  psu) CDW. These two water masses are separated by a pycnocline, where the  $T$ - $S$  properties lie along an approximately straight line between CDW and WW (Figure 5a). Meanwhile, the temperature and salinity of any water masses generated by melting of glacial ice should lie on a straight line with a typical slope of  $\sim 2.7 \text{ } ^\circ\text{C psu}^{-1}$  (the meltwater mixing line) passing through the temperature and salinity of the water mass that is the source water for melting [Gade, 1979; Greisman, 1979]. In the PIG ice-shelf cavity, the source water for melting is largely CDW with some contribution from pycnocline water (Figure 5a).

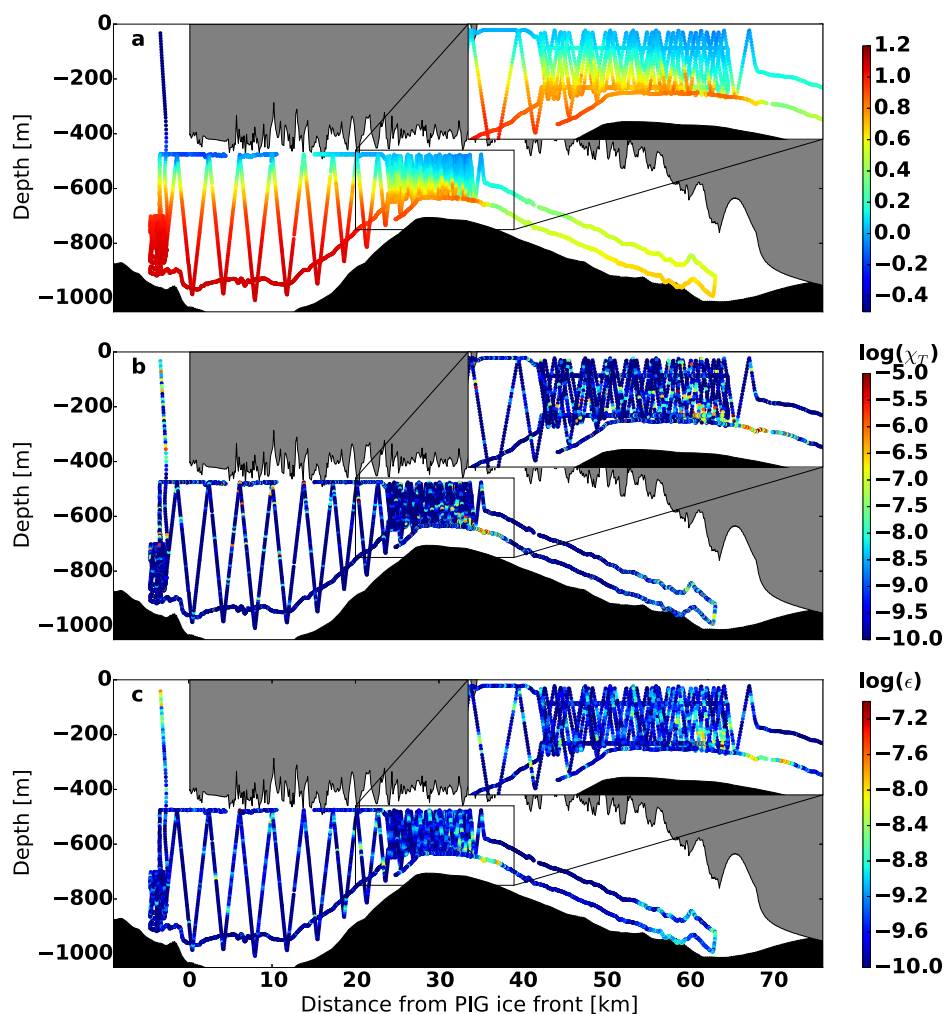


**Figure 4.** (a) Potential temperature, (b)  $\chi_T$ , (c)  $\epsilon$  from the AUV track A and B. The ice draft and seabed depth are derived from the 2009 ADCP range data along track A.

The pycnocline water occupies the upper part of the cavity between 0 and 20 km away from the ice front, and  $\epsilon$  along the meltwater mixing line in this area is equivalent to the open-ocean background level  $O(10^{-10}) \text{ W kg}^{-1}$  (Figure 5b). The warmest CDW in the cavity ( $T \sim 1^\circ \text{C}$ ) does not penetrate beyond 28 km away from the ice front, and the  $T$ - $S$  properties farther from the calving front are characterized by the mixture of meltwater and thermocline water (Figure 5c). A cluster of elevated  $\epsilon$  between  $10^{-8}$  and  $10^{-7} \text{ W kg}^{-1}$  is found along  $\sigma_\theta = 27.65 \text{ kg m}^{-3}$ , located near the seabed over the crest of the ridge, where the thermocline water interacts with the water from the onshore side of the ridge (Figure 5c). Many measurements of  $\epsilon$  on oceanic flows over a ridge have been made [e.g., Rudnick *et al.*, 2003; Sheen *et al.*, 2014], and our measurements of  $\epsilon$  are of similar magnitude. As the AUV approaches closer to the eastern grounding line ( $>32$  km away from the calving front),  $T$ - $S$  properties lie along the meltwater mixing line, and high  $\epsilon$  is observed, suggesting elevated mixing of meltwater near the grounding line (Figure 5d).

#### 4. Observations Across the Ice Flow From the Ridge Crest to the Southern Grounding Line (Autosub Track C)

The ice base morphology in the direction transverse to the ice flow has channels and steps, and the track C collected data across these structures (Figure 6). The water column thickness beneath the ice shelf varies between 120 and 620 m, and the ice keels between channels are exposed to warmer water (Figure 6a). The presence of the warm water near the ice implies high temperature gradients and indeed  $\chi_T$  tends to

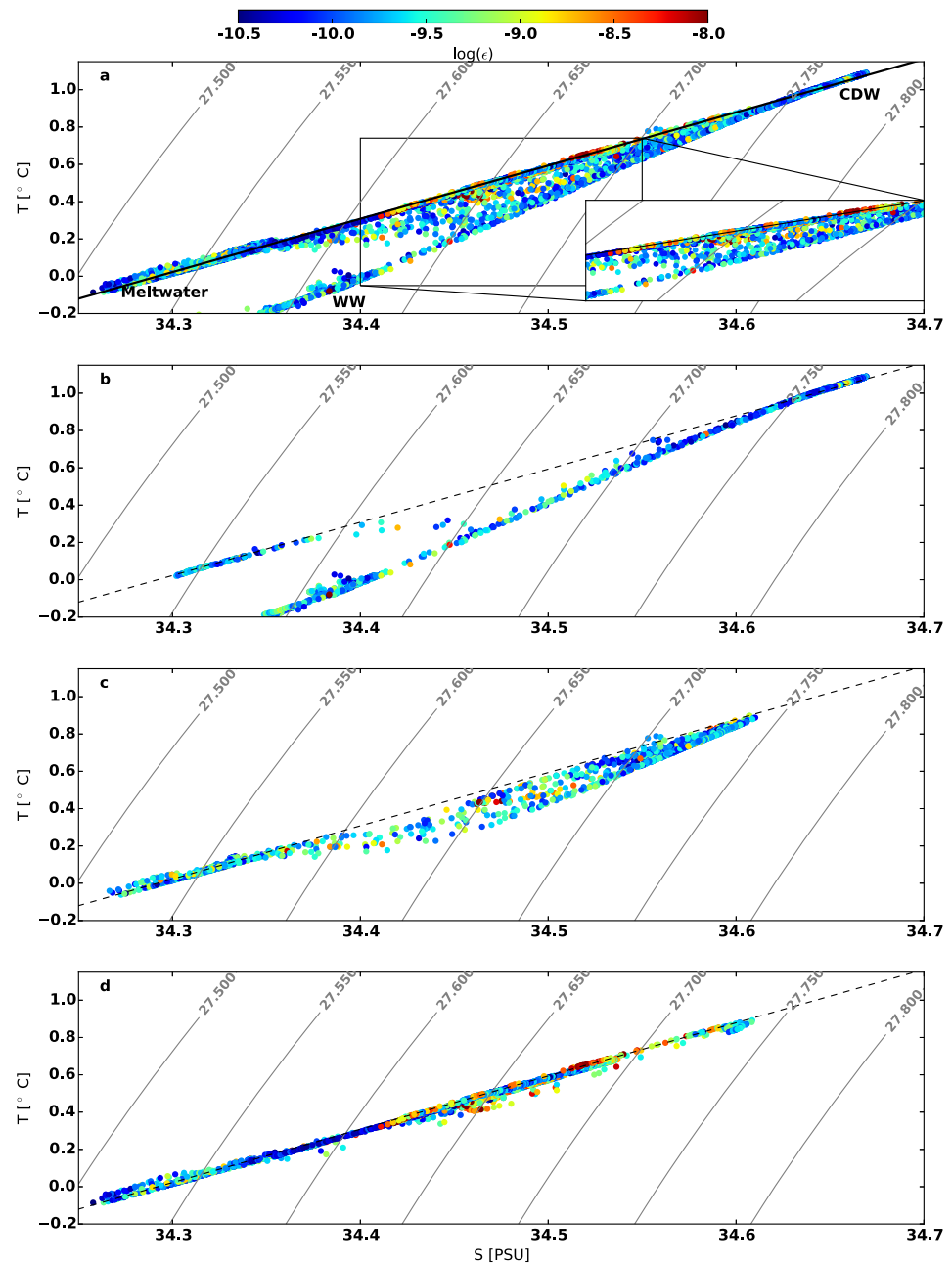


**Figure 5.** (a)  $T$ - $S$  diagram from all the AUV observations in 2014. The color indicates  $\log(\epsilon)$ , and the solid line is a meltwater mixing line.  $T$ - $S$  diagram of selected regions (b) seaward side of the cavity between 0 and 20 km away from the ice front, (c) crest of the ridge, between 28 and 32 km away from the ice front, (d) inshore side of the ridge, >32 km away from the ice front.

increase near the keels (Figure 6b). The highest  $\epsilon$  of  $1.35 \times 10^{-7} \text{ W kg}^{-1}$  is observed near the ice-shelf base and approximately 2 km away from the southern grounding line; this  $\epsilon$  is an order of magnitude larger than at the crest of the ridge (Figure 6c).

A sharp temperature gradient is maintained within 20 m of the ice shelf (Figure 7a). During the horizontal track in the vicinity of the ice, the average temperature was  $-0.41 \text{ }^\circ\text{C}$ ,  $1.76 \text{ }^\circ\text{C}$  above the in situ freezing point; the standard deviation was  $0.12 \text{ }^\circ\text{C}$ . The horizontal current speed within 40 m of the ice shelf is relatively slow,  $0.07 \text{ m s}^{-1}$  with speed decreasing from 0 to 20 m and increasing over 20–40 m from the ice. The  $\epsilon$  and  $\chi_T$  increase up to  $6.2 \times 10^{-8} \text{ W kg}^{-1}$  and  $2 \times 10^{-5} \text{ }^\circ\text{C}^2 \text{ s}^{-1}$  (Figure 7c). The maximum  $\epsilon$  is found just after the AUV

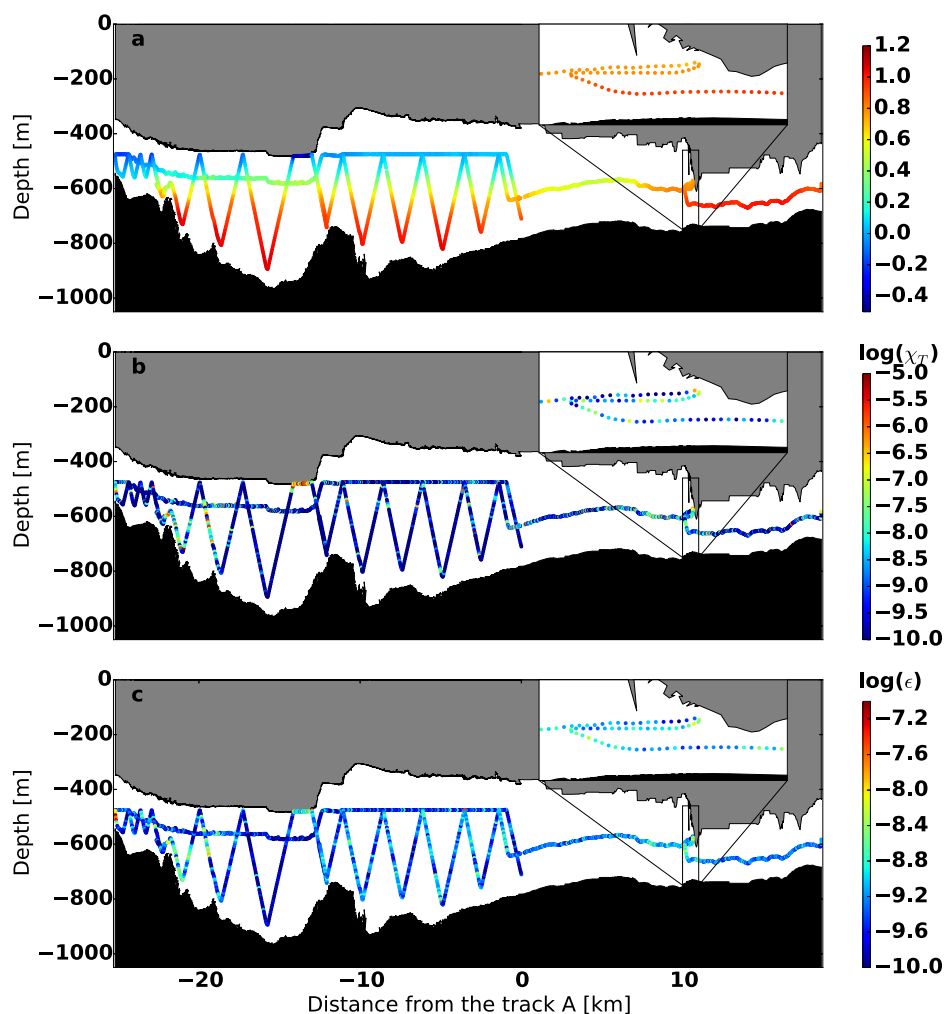


**Figure 6.** (a) Potential temperature, (b)  $\chi_T$ , (c)  $\epsilon$  from the track C, across the ice flow looking out to sea. The horizontal axes indicate the distance from the intersection of the tracks A and C (see Figure 1), and the vertical axes is the depth. The ice draft and bed depth are derived from the AUV's sonar device.

reached the keel of the ice shelf (the AUV's horizontal travelling distance of  $\sim 2000$  m in Figure 7c), whereas the maximum  $\chi_T$  is confined near the ice base. The location of maximum  $\epsilon$  suggests that the flow becomes energetic near the keel of the ice shelf.

## 5. Discussion

Oceanic values of  $\epsilon$  have a wide range, spanning about 10 orders of magnitude from  $10^{-11}$  W kg $^{-1}$  in the abyssal ocean up to  $10^{-1}$  W kg $^{-1}$  in the regions of extremely active mixing, e.g., surf zone and fast tidal zone; however in the ocean interior they are generally up to  $10^{-7}$  W kg $^{-1}$ . Prior to this study, there were no measurements to confirm the range of  $\epsilon$  beneath an ice shelf. Our measurements reveal that the range of  $\epsilon$  beneath PIG ice shelf extends from the background value of  $10^{-10}$  W kg $^{-1}$  up to  $10^{-7}$  W kg $^{-1}$ . The highest  $\epsilon$  of  $1.35 \times 10^{-7}$  W kg $^{-1}$  was observed at the closest approach to the southern grounding line. Elevated mixing was also found at the crest of the ridge and near the ice base, where high temperature gradient is maintained by the contact with glacial meltwater.

Despite widespread interest in understanding how oceanic turbulence distributes momentum, heat, and salt at the ice-ocean interface, direct flux measurements within the ice-shelf-ocean boundary layer are rare, mostly due to the difficulty in gaining access through the ice shelf. The basal melting of ice shelves is not

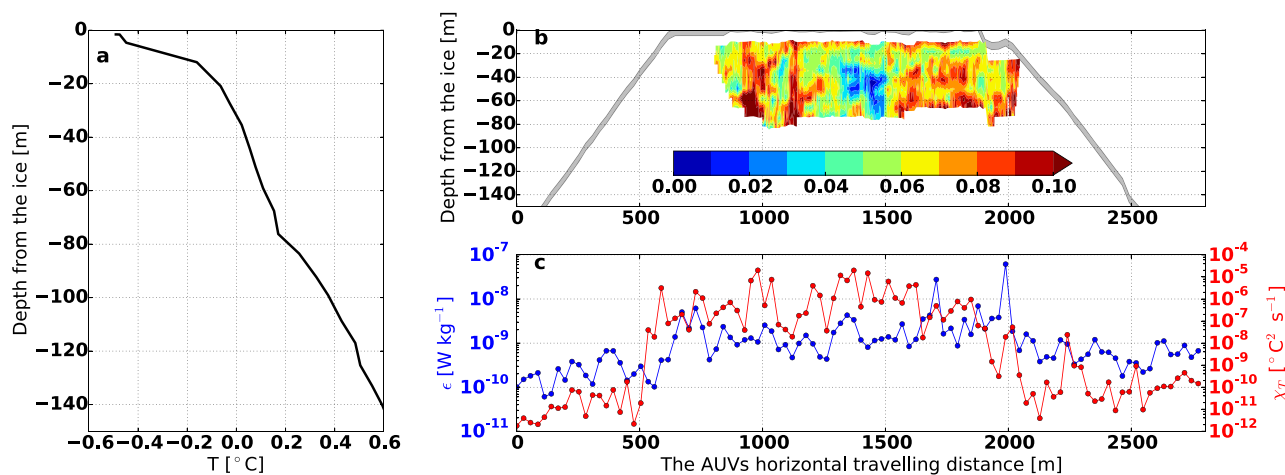


**Figure 7.** Oceanic conditions in the vicinity of the ice, the segment of transect between  $-15$  and  $-12$  km in Figure 6. (a) The solid dark line indicates the temperature profiles during the ascend cast. (b) The water speed,  $\text{m s}^{-1}$ , derived from the ADCP is color coded, during up, horizontal and down casts. The shaded region indicates the AUV track. During the horizontal cast, the AUV traveled within 1 m of the ice shelf. (c)  $\epsilon$  (blue) and  $\chi_T$  (red) measurements over this section of the AUV track.

easy to parameterize, due to our lack of understanding of the turbulent transports within the ice-shelf-ocean boundary layer, as well as the fact that the flow condition beneath ice shelves varies between different ice shelves. Direct oceanographic measurements beneath ice shelves have revealed both high and low Reynolds number regimes. Observations beneath ice shelves surrounded by water that is near in situ freezing point, such as Filchner-Ronne, Larsen C, and Ross ice shelves, suggest that the flow is in the high Reynolds number regime as a result of the large-scale circulation, modulated by tidal motion [Jacobs *et al.*, 1979; Nicholls and Jenkins, 1993]. In contrast, distinct signatures of thermohaline staircases (a stack of well-mixed layers separated by sharp interfaces) were seen in the profiles beneath George VI Ice Shelf in the Bellingshausen Sea, Antarctica, indicating possible low Reynolds number flow [Kimura *et al.*, 2015]. In the rest of this section, we will use the direct measurements of  $\epsilon$  described in the previous section to estimate basal melt rate.

### 5.1. Estimation of $u_*$ From $\epsilon$ Near the Ice Base

The turbulent transport of momentum, heat and salt can be parameterized in term of a friction velocity,  $u_*$ , associated with the Reynolds stress in the boundary layer. Such a parameterization is routinely employed in general circulation models (GCMs) in order to estimate ice-shelf melt rates [e.g., Holland and Jenkins, 2001; Losch, 2008; Holland *et al.*, 2008; Little *et al.*, 2009].

In a steady stratified shear flow, the rate of turbulent kinetic energy production by the Reynolds stress,  $\tau$ , working against the mean shear (shear production term) is balanced by the turbulent kinetic energy dissipation rate and buoyancy production term:

$$\frac{\tau}{\rho} \cdot \frac{dU}{dz} = \epsilon - \overline{w'b'}, \quad (1)$$

where  $\rho$  is the density of seawater,  $dU/dz$  is the background mean shear, and  $w'$  and  $b'$  are vertical velocity and buoyancy fluctuations, respectively. The appropriate Reynolds stress is defined by the covariance of horizontal and vertical velocity fluctuations as

$$\tau = -\overline{\rho u'w'}, \quad (2)$$

where  $w'$  is the horizontal velocity fluctuation [Tennekes and Lumley, 1972]. A nondimensionalized mean shear  $\phi_m$  can be expressed as

$$\phi_m = \frac{\kappa z}{u_*} \frac{dU}{dz}, \quad (3)$$

where  $\kappa$  and  $z$  represent von Kármán's constant and distance from the ice, respectively. Measurements of  $\kappa$  in marine environments are approximately equal to 0.4 [Soulsby, 1983]. The variable  $u_*$  represents the friction velocity that can be expressed as

$$u_* = \sqrt{\frac{|\tau|}{\rho}} \tag{4}$$

Several forms of  $\phi_m$  have been suggested. In the absence of the stratification, the mixing length depends only on distance from the ice,  $z$ , following the mixing length argument of Prandtl, thereby

$$\phi_m = 1. \tag{5}$$

In this case, integration of (3) yields the law of the wall, which states that the mean velocity of the turbulent flow,  $U(z)$ , is proportional to the logarithm of the distance from the wall:  $U = \frac{u_*}{\kappa} \ln\left(\frac{z}{z_0}\right)$ , where  $z_0$  is a constant of integration such that  $U(z_0) = 0$  and represents a length scale proportional to the roughness of the ice base.

For a stably stratified boundary layer, *Monin and Obukhov* [1954] argued that  $\phi_m$  is a function of the nondimensional height  $\xi = z/L_o$ . The variable  $L_o$  is the Obukhov length, defined as

$$L_o = -\frac{u_*^3}{\kappa w' b'} \tag{6}$$

The Obukhov length,  $L_o$ , represents the height at which the buoyancy production of turbulence kinetic energy is equal to the shear production. Within  $L_o$  from the wall, the shear production dominates over the buoyancy production. The value of  $L_o$  can provide a practical measure of the deviation from statically neutral state with decreasing  $L_o$  corresponding to larger deviation from the neutral state.

Studies of the atmospheric boundary layer have found that to first order

$$\phi_m(\xi) = 1 + \gamma \xi, \tag{7}$$

where  $\gamma$  is an empirically determined parameter, which varies widely from 0.6 to near 5 [e.g., *Halstead*, 1943; *Businger et al.*, 1971; *Dyer*, 1974]. We express  $u_*$  in terms of  $\epsilon$  and  $\overline{w' b'}$  by substituting (3) and (4) into (1):

$$u_* = [\kappa z (\epsilon - (1 - \gamma) \overline{w' b'})]^{1/3} \tag{8}$$

The stabilizing buoyancy production associated with melting ice is

$$\overline{w' b'} = g m' \left[ \alpha \left( (T_\infty - T_b) + \frac{L}{c_p} + \frac{c_l}{c_p} (T_b - T_l) \right) - \beta S_\infty \right], \tag{9}$$

where  $\alpha$  and  $\beta$  are the thermal expansion and saline contraction coefficients (Appendix A). The “far-field” ocean temperature and salinity are represented by  $T_\infty$  and  $S_\infty$ . The variables  $g = 9.81 \text{ m s}^{-2}$ ,  $c_p = 3974 \text{ J kg}^{-1} \text{ }^\circ\text{C}^{-1}$ , and  $L = 3.35 \times 10^5 \text{ J kg}^{-1}$  represent the gravity, specific heat capacity of seawater, and latent heat of ice fusion, respectively. The direction of ice melting does not necessary have to be aligned with the vertical coordinate of the ocean, and  $m'$  represents the velocity of the ocean in the direction normal to the ice-ocean interface. The melt rate of ice is  $m = \rho m' / \rho_{ice}$ , where  $\rho_{ice}$  is the density of ice. The  $m'$  is determined by the three-equation model, which links the local freezing relation and the balance of heat and salt fluxes at the ice-ocean interface [*Holland and Jenkins*, 1999]. The local freezing relation constrains the temperature  $T_b$  and salinity  $S_b$  at the ice-ocean interface:

$$T_b = a S_b + b + c P, \tag{10}$$

where  $a = -0.0573 \text{ }^\circ\text{C}$ ,  $b = 0.0832 \text{ }^\circ\text{C}$ , and  $c = -7.53 \times 10^{-8} \text{ }^\circ\text{C Pa}^{-1}$ , and  $P$  is the local hydrostatic pressure. The balances of heat and salt fluxes between the ice and ocean are

$$m' L + m' c_l (T_b - T_l) = c_p \gamma_T u_* (T_\infty - T_b) \quad \text{and} \tag{11}$$

$$m' S_b = \gamma_S u_* (S_\infty - S_b), \tag{12}$$

where  $T_l = -25 \text{ }^\circ\text{C}$  and  $c_l = 2009 \text{ J kg}^{-1} \text{ }^\circ\text{C}^{-1}$  are the internal temperature and specific heat capacity of ice. The variables  $\gamma_T$  and  $\gamma_S$  are the nondimensional exchange coefficients of the heat and salt transfer through the boundary layer. Assuming the ice-ocean interface to be hydraulically smooth surface, the nondimensional exchange coefficients take forms [*Kader and Yaglom*, 1972]:

$$\gamma_T = \frac{1}{2.12 \ln(u_* h / \nu) + 12.5 Pr^{2/3} - 9} \quad (13)$$

and

$$\gamma_S = \frac{1}{2.12 \ln(u_* h / \nu) + 12.5 Sc^{2/3} - 9}, \quad (14)$$

where  $Pr$  and  $Sc$  are the molecular Prandtl (the ratio of viscosity to thermal diffusivity) and Schmidt number (the ratio of viscosity to saline diffusivity), respectively. The variable,  $h$  indicates the thickness of the boundary layer. The first term in the denominator is the turbulence contribution to the exchange coefficient and the second term is the molecular contribution. The presence of stratification suppresses the turbulence, and we expect the contribution from the turbulence to decrease. In a statically neutral state, the thickness of the viscous sublayer is  $5\nu/u_*$  [Tennekes and Lumley, 1972], so we estimate the upper bound for the turbulence contribution to be 3.4. In polar oceans, the  $Pr$  and  $Sc$  are  $\sim 13.8$  and  $\sim 2432$ , so the second term representing the molecular contribution is 63 and 2252 for heat and salt, respectively, at least an order of magnitude and three orders of magnitude larger than the contribution from the turbulence. In the following discussion, we assume the molecular contributions dominate in the exchange coefficients:  $\gamma_T = 1.6 \times 10^{-2}$  and  $\gamma_S = 4.4 \times 10^{-4}$ . The three equations (10–12), combined with (8) and (9), are solved simultaneously to compute the three unknowns  $m'$ ,  $T_b$ , and  $S_b$  from given  $T_\infty$ ,  $S_\infty$ , and  $\epsilon$ . A procedure to solve the equations is outlined in Appendix B. The “far-field” ocean temperature and salinity are combined to calculate the thermal driving:

$$T_* = T_\infty - (aS_\infty + b + cP). \quad (15)$$

## 5.2. Estimate of $u_*$ and Its Effect on Melt Rate, $m$

The key to a consistent ice-shelf-ocean boundary layer parameterization lies in the choice of the friction velocity. Our measurement shows that average and maximum  $\epsilon$  near the ice base ( $\sim 0.5$  m below ice) are  $3.5 \times 10^{-9}$  and  $6.2 \times 10^{-8}$   $\text{W kg}^{-1}$ . The thermal driving is between 1.6 and 2.2  $^\circ\text{C}$ . From these observations near the ice base, we estimate  $u_*$ ,  $m$ , and  $L_o$ . One of the uncertainties lies in the choice of  $\gamma$ , the stability correction parameter for the nondimensional mean shear in (7). The empirical values of  $\gamma$  come from the measurements of the diurnal buoyancy cycle within the atmospheric boundary layer in the midlatitude. The diurnal buoyancy forcing is likely to have a greater impact on the atmospheric boundary layer than the melting ice has on the ice-ocean boundary layer. In sea ice-ocean boundary layer, *McPhee* [2008] argues that neutral scaling ( $\gamma = 0$ ) would most likely be appropriate for ice packs away from marginal ice zones or large polynyas and suggests  $\gamma$  between 0 and 3 for Arctic sea ice. Here we consider  $\gamma$  between 0 and 3.

The  $u_*$ ,  $m$ , and  $L_o$  inversely scale with the choice of  $\gamma$ , so the estimates are sensitive to  $\gamma$ . Our estimates of  $u_*$  are between 0.0015 and 0.0037  $\text{m s}^{-1}$  for  $\gamma = 0$  and  $\gamma = 0.6$ , and the estimate decreases down to  $4 \times 10^{-6}$   $\text{m s}^{-1}$  when  $\gamma = 3$  (Figure 8a). Decreasing  $u_*$  with increasing  $\gamma$  is consistent with the idea that the presence of stratification suppresses the turbulence, thereby reducing the friction velocity. The uncertainties in the estimates decrease with increasing  $\epsilon$  (Figure 8b). The relative contribution from the buoyancy production term to  $u_*$  decreases with increasing  $\epsilon$ , and the choice of  $\gamma$  becomes less important in high  $\epsilon$ .

Based on  $\epsilon$ , we estimate the melt rate of this region to be between 10 and 29  $\text{m yr}^{-1}$  for  $\gamma = 0$  and  $\gamma = 0.6$  and down to 0.03  $\text{m yr}^{-1}$  for  $\gamma = 3$  (Figure 8c). The melt rate increases with increasing  $\epsilon$  as more energy is available to bring heat to the ice base (Figure 8d). These estimates are based on point measurements, and we do not have direct measurements of the basal melt rate to verify this calculation. Nevertheless historical measurements based on the oceanic-heat budget can provide us a clue on the reliability of our estimates. The first measurement of Pine Island Bay in 1994 indicated that the basal melt rate in PIG ice shelf was  $12 \pm 3$   $\text{m yr}^{-1}$  [Jacobs et al., 1996], and this estimate was consistent with the glacier mass balance of upstream input, frontal calving and surface mass balance, derived from satellite and in situ observations [Jenkins et al., 1997]. Recent measurements have shown that the basal melt rate decreased from 18 to 11  $\text{m yr}^{-1}$  between 2009 and 2012 [Dutrieux et al., 2014a]; however, spatial variations in basal melt rates can be quite large. Satellite and airborne measurements between 2008 and 2009 have revealed up to 100  $\text{m yr}^{-1}$  near the eastern grounding line and reduction down to 30  $\text{m yr}^{-1}$  just 20 km downstream [Dutrieux et al., 2013]. The ice comes in contact with the warmest waters near the grounding line so high melting near the

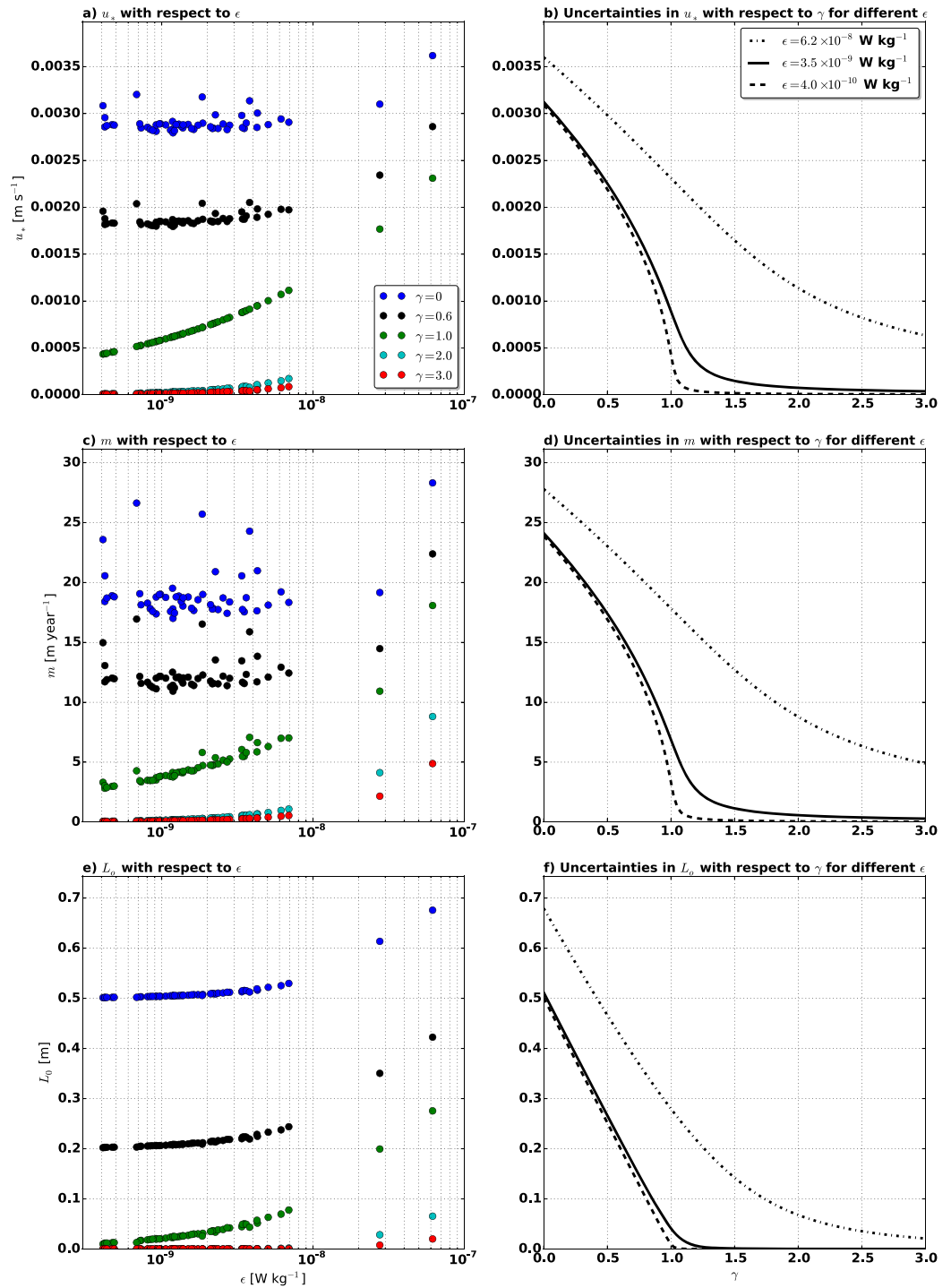


**Figure 8.** (a) Comparison of the friction velocity, (c) melt rate, and (e) Obukhov length estimated from our observations with respect to  $\epsilon$  for different values of  $\gamma$ . (b) Sensitivity of the friction velocity, (d) melt rate, and (f) Obukhov length by the choice of  $\gamma$  for three different  $\epsilon$ . Our observations of  $\epsilon$  range from  $4.0 \times 10^{-10}$  to  $6.2 \times 10^{-8}$  W kg $^{-1}$  with the mean of  $3.5 \times 10^{-9}$  W kg $^{-1}$ .

grounding line [Jenkins et al., 2010]. The direct measurements of basal melt rates from five sites (within 1 km of each other) in 2012 indicate less than  $0.37$  m yr $^{-1}$  from one site and  $14$ – $22$  m yr $^{-1}$  from other four sites [Stanton et al., 2013]. These measurements suggest that our estimate of basal melt rates is within a reasonable range.

The estimates of  $L_o$  are based on  $u_*$  and  $m$  as defined in (6) and (9). The estimates range from nearly zero up to 0.7 m (Figure 8e). More mechanical energy is available for higher  $\epsilon$ , increasing the shear production term, and therefore  $L_o$  increases with increasing  $\epsilon$  (Figure 8f). The production of the turbulent kinetic energy by the shear production is confined within 0.7 m from the ice, which suggests the importance of incorporating the turbulence kinetic energy production by the buoyancy production term from melting ice.

### 6. Conclusions

We have analyzed turbulence data collected by an AUV from PIG ice-shelf cavity. In light of these observations, we estimated the friction velocity and melt rate from  $\epsilon$ . Our main findings are as follows:

1. The highest  $\epsilon=O(10^{-7})$  is observed when the AUV is the closest to the grounding line (2 km away from the southern part of the grounding line), where the outflow of meltwater occurs. Another region of high  $\epsilon$  is found over the ridge where a high density gradient is maintained by the baroclinic front between the modified CDW and meltwater.
2. Our measurements show that average  $\epsilon$  and  $\chi_T$  near the ice base are  $3 \times 10^{-9} \text{ W kg}^{-1}$  and  $2.3 \times 10^{-6} \text{ }^\circ\text{C}^2 \text{ s}^{-1}$ , respectively. The maximum  $\epsilon$  of  $6.2 \times 10^{-8} \text{ W kg}^{-1}$  is found near the keel of the ice shelf, and high  $\chi_T$  up to  $2 \times 10^{-5} \text{ }^\circ\text{C}^2 \text{ s}^{-1}$  is confined near the ice base. From these measurements, we have estimated the melt rate assuming that the shear production is balanced by the combination of turbulent dissipation  $\epsilon$  and the buoyancy flux from melting ice. This assumption constrains the friction velocity and melt rate to depend on  $\epsilon$ . We have derived friction velocity and melt rate for two different forms of nondimensional mean shear,  $\phi_m(\xi)=1$  (statically neutral boundary layer) and  $\phi_m(\xi)=1+\gamma\xi$  (stably stratified boundary layer) with  $\gamma$  ranging up to 3. Assuming the statically neutral boundary layer, the melt rate estimates range from 17 to 28  $\text{m yr}^{-1}$ . The estimate decreases with increasing  $\gamma$  down to  $0.03 \text{ m yr}^{-1}$ . Improved understanding of nondimensional mean shear for the ice-shelf-ocean boundary (a precise value of  $\gamma$  or other forms of the nondimensional shear) is needed to better constrain the melt rate estimate.
3. The estimated Obukhov length scale, from friction velocity derived from our measured  $\epsilon$ , is at most 0.7 m, i.e., the production of turbulent kinetic energy by shear production is dominant only within 0.7 m of the ice-ocean interface. Below the depth of Obukhov length, stabilizing buoyancy flux from ice melting dominates the production of turbulent kinetic energy. This implies that estimates of friction velocity for parameterizations of basal melt rate must consider the production of turbulent kinetic energy by ice melting.

### Appendix A: Derivation of $\overline{w'b'}$

The buoyancy flux associated with melting of ice shelf ( $\overline{w'b'}$ ) is related to the density deficit within the ice-ocean boundary layer,  $\Delta\rho$ :

$$\overline{w'b'} = -gm'\Delta\rho, \quad \text{where} \quad \Delta\rho = -\alpha(T_\infty - T) + \beta(S_\infty - S). \tag{A1}$$

The variables  $T$  and  $S$  are temperature and salinity within the ice-ocean boundary layer,

$$T = T_b - \frac{\gamma_T u_* (T_\infty - T_b)}{m'} \quad \text{and} \quad S = S_b - \frac{\gamma_S u_* (S_\infty - S_b)}{m'}, \tag{A2}$$

where  $T_b$  and  $S_b$  are the temperature and salinity at the ice/ocean interface. The second terms  $\frac{\gamma_T u_* (T_\infty - T_b)}{m'}$  and  $\frac{\gamma_S u_* (S_\infty - S_b)}{m'}$  represent the oceanic contribution of temperature and salinity. We now rewrite (A2) using (11) and (12),

$$T = T_b - \frac{L}{c_p} - \frac{c_l}{c_p} (T_b - T_l) \quad \text{and} \quad S = 0. \tag{A3}$$

Substitutions of the above expressions into (A1) gives

$$\overline{w'b'} = gm' \left[ \alpha \left( T_\infty - T_b + \frac{L}{c_p} + \frac{c_l}{c_p} (T_b - T_l) \right) - \beta S_\infty \right]. \tag{A4}$$

## Appendix B: A Procedure to Solve the Three-Equation Model in Section 5

Our objective is to solve three unknowns,  $S_b$ ,  $T_b$ , and  $m'$ , from the three equations (10–12). We combine (11) and (12) to reduce the problem into two unknowns  $T_b$  and  $S_b$ , and the quadratic equation for  $S_b$  is derived by expressing  $T_b$  in terms of  $S_b$  by (10):

$$AS_b^2 + BS_b + C = 0. \quad (B1)$$

The solution for  $S_b$  is

$$S_b = \frac{-B \pm \sqrt{B^2 - 4AC}}{2A}, \quad (B2)$$

where

$$A = a(c_p \gamma_T - \gamma_S c_l), \quad B = \gamma_S (S_\infty c_l a - L) - \gamma_S c_l (b + cP - T_l) + c_p \gamma_T (b + cP - T_\infty) \quad (B3)$$

and

$$C = \gamma_S S_\infty (L + c_l (b + cP - T_l)). \quad (B4)$$

The variables A, B and C do not contain any unknowns. Once the  $S_b$  is determined,  $T_b$  is computed by the freezing relationship (10).

We are now left to determine  $m'$  from solving (12). The expression for  $u_*$  in terms of  $m'$  is

$$u_* = \left[ \kappa z \left( \epsilon - (1 - \gamma) g m' \left[ \alpha \left( (T_\infty - T_b) + \frac{L}{c_p} + \frac{c_l}{c_p} (T_b - T_l) \right) - \beta S_\infty \right] \right) \right]^{\frac{1}{3}}. \quad (B5)$$

Substituting (B5) into (12) gives

$$(m' S_b)^3 = \gamma_S^3 (S_\infty - S_b)^3 \kappa z \left[ \epsilon - (1 - \gamma) g m' \left[ \alpha \left( (T_\infty - T_b) + \frac{L}{c_p} + \frac{c_l}{c_p} (T_b - T_l) \right) - \beta S_\infty \right] \right]. \quad (B6)$$

When the far-field salinity is equal to the salinity at the ice-ocean interface ( $S_\infty = S_b$ , implying  $T_* = 0$ ), the ice does not melt ( $m' = 0$ ). Rearranging the above equations results in a cubic equation for  $m'$ :

$$m'^3 + \frac{\kappa z \gamma_S^3 (S_\infty - S_b)^3}{S_b^3} (1 - \gamma) g m' \left[ \alpha \left( (T_\infty - T_b) + \frac{L}{c_p} + \frac{c_l}{c_p} (T_b - T_l) \right) - \beta S_\infty \right] - \kappa z \epsilon \frac{\gamma_S^3 (S_\infty - S_b)^3}{S_b^3} = 0. \quad (B7)$$

The cubic equation is numerically solved to determine  $m'$  from given  $T_\infty$ ,  $S_\infty$ , and  $\epsilon$ .

### Acknowledgments

The authors thank the captain and crews of *RRS James Clark Ross*. This work was supported by funding from the UK Natural Environment Research Council's iSTAR Programme (NERC Grant Number NE/J005770/1 and NE/J005746/1). The data for this study are available upon request to the corresponding author (Satoshi Kimura, skimura04@gmail.com).

### References

- Alley, K. E., T. A. Scambos, M. R. Siegfried, and H. A. Fricker (2016), Impacts of warm water on Antarctic ice shelf stability through basal channel formation, *Nat. Geosci.*, *9*(4), 290–293.
- Assmann, K. M., A. Jenkins, D. R. Shoosmith, D. P. Walker, S. S. Jacobs, and K. W. Nicholls (2013), Variability of Circumpolar Deep Water transport onto the Amundsen Sea Continental shelf through a shelf break trough, *J. Geophys. Res. Oceans*, *118*, 6603–6620, doi:10.1002/2013JC008871.
- Bamber, J. L., R. E. M. Riva, B. L. A. Vermeersen, and A. M. LeBrocq (2009), Reassessment of the potential sea-level rise from a collapse of the West Antarctic Ice Sheet, *Science*, *324*(5929), 901–903, doi:10.1126/science.1169335.
- Batchelor, G. K. (1959), Small-scale variation of convected quantities like temperature in turbulent fluid. Part 1: General discussion and the case of small conductivity, *J. Fluid Mech.*, *5*(01), 113–133.
- Businger, J. A., J. C. Wyngaard, Y. Izumi, and E. F. Bradley (1971), Flux-profile relationships in the atmospheric surface layer, *J. Atmos. Sci.*, *28*(2), 181–189.
- De Rydt, J., P. R. Holland, P. Dutrieux, and A. Jenkins (2014), Geometric and oceanographic controls on melting beneath Pine Island Glacier, *J. Geophys. Res. Oceans*, *119*(4), 2420–2438, doi:10.1002/2013JC009513.
- Dutrieux, P., D. G. Vaughan, H. F. J. Corr, A. Jenkins, P. R. Holland, I. Joughin, and A. H. Fleming (2013), Pine Island glacier ice shelf melt distributed at kilometre scales, *Cryosphere*, *7*(5), 1543–1555, doi:10.5194/tc-7-1543-2013.
- Dutrieux, P., J. De Rydt, A. Jenkins, P. R. Holland, H. K. Ha, S. H. Lee, E. J. Steig, Q. Ding, E. P. Abrahamson, and M. Schröder (2014a), Strong sensitivity of Pine island ice-shelf melting to climatic variability, *Science*, *343*(6167), 174–178.
- Dutrieux, P., C. Stewart, A. Jenkins, K. W. Nicholls, H. F. J. Corr, E. Rignot, and K. Steffen (2014b), Basal terraces on melting ice shelves, *Geophys. Res. Lett.*, *41*, 5506–5513, doi:10.1002/2014GL060618.
- Dyer, A. J. (1974), A review of flux-profile relationships, *Boundary Layer Meteorol.*, *7*(3), 363–372, doi:10.1007/BF00240838.
- Favier, L., G. Durand, S. L. Cornford, G. H. Gudmundsson, O. Gagliardini, F. Gillet-Chaulet, T. Zwinger, A. J. Payne, and A. M. Le Brocq (2014), Retreat of Pine Island Glacier controlled by marine ice-sheet instability, *Nat. Clim. Change*, *4*(2), 117–121.

- Gade, H. G. (1979), Melting of ice in sea water: A primitive model with application to the Antarctic ice shelf and icebergs, *J. Phys. Oceanogr.*, *9*, 189–198.
- Greisman, P. (1979), On upwelling driven by the melt of ice shelves and tidewater glaciers, *Deep Sea Res., Part A*, *26*(9), 1051–1065.
- Gudmundsson, G. H. (2013), Ice-shelf buttressing and the stability of marine ice sheets, *Cryosphere*, *7*(2), 647–655, doi:10.5194/tc-7-647-2013.
- Halstead, M. (1943), A stability-term in the wind-gradient equation, *Eos Trans. AGU*, *24*(1), 204–208, doi:10.1029/TR024i001p00204.
- Holland, D. M., and A. Jenkins (1999), Modeling thermodynamic ice–ocean interactions at the base of an ice shelf, *J. Phys. Oceanogr.*, *29*, 1787–1800.
- Holland, D. M., and A. Jenkins (2001), Adaptation of an isopycnic coordinate ocean model for the study of circulation beneath ice shelves, *Mon. Weather Rev.*, *129*, 1905–1927.
- Holland, P. R., A. Jenkins, and D. M. Holland (2008), The response of ice shelf basal melting to variations in ocean temperature, *J. Clim.*, *21*(11), 2558–2572, doi:10.1175/2007JCLI1909.1.
- Jacobs, S. S., A. L. Gordon, and J. L. Ardial Jr. (1979), Circulation and melting beneath the Ross Ice Shelf, *Science*, *203*, 441–443.
- Jacobs, S. S., H. H. Hellmer, and A. Jenkins (1996), Antarctic ice sheet melting in the southeast Pacific, *Geophys. Res. Lett.*, *23*, 957–960.
- Jacobs, S. S., A. Jenkins, C. F. Giulivi, and P. Dutrieux (2011), Stronger ocean circulation and increased melting under Pine Island Glacier ice shelf, *Nat. Geosci.*, *4*(8), 519–523.
- Jenkins, A., D. G. Vaughan, S. S. Jacobs, H. H. Hellmer, and J. R. Keys (1997), Glaciological and oceanographic evidence of high melt rates beneath Pine Island Glacier, West Antarctica, *J. Glaciol.*, *43*, 114–121.
- Jenkins, A., P. Dutrieux, S. Jacobs, S. McPhail, J. Perrett, A. Webb, and D. White (2010), Observations beneath Pine Island Glacier in West Antarctica and implications for its retreat, *Nat. Geosci.*, *3*, 468–472.
- Joughin, I., E. Rignot, C. E. Rosanova, B. K. Lucchitta, and J. Bohlander (2003), Timing of recent accelerations of Pine island glacier, Antarctica, *Geophys. Res. Lett.*, *30*(13), 1706, doi:10.1029/2003GL017609.
- Joughin, I., B. E. Smith, and B. Medley (2014), Marine ice sheet collapse potentially under way for the Thwaites glacier basin, west Antarctica, *Science*, *344*(6185), 735–738.
- Kader, B., and A. Yaglom (1972), Heat and mass transfer laws for fully turbulent wall flows, *Int. J. Heat Mass Transfer*, *15*, 2329–2351.
- Kimura, S., K. W. Nicholls, and E. Venables (2015), Estimation of ice shelf melt rate in the presence of a thermohaline staircase, *J. Phys. Oceanogr.*, *45*(1), 133–148, doi:10.1175/JPO-D-14-0106.1.
- Levine, E. R., and R. G. Lueck (1999), Turbulence measurement from an autonomous underwater vehicle, *J. Atmos. Oceanic Technol.*, *16*, 1533–1544.
- Little, C. M., A. Gnanadesikan, and M. Oppenheimer (2009), How ice shelf morphology controls basal melting, *J. Geophys. Res.*, *114*, C12007, doi:10.1029/2008JC005197.
- Losch, M. (2008), Modeling ice shelf cavities in a z-coordinate ocean general circulation model, *J. Geophys. Res.*, *113*, C08043, doi:10.1029/2007JC004368.
- McPhee, M. (2008), *Air-Ice-Ocean Interaction*, Springer, Berlin.
- Monin, A., and A. Obukhov (1954), Basic laws of turbulent mixing in the surface layer of the atmosphere, *Tr. Akad. Nauk SSSR Geophys. Inst.*, *24*(151), 163–187.
- Nicholls, K. W., and A. Jenkins (1993), Temperature and salinity beneath Ronne ice shelf, Antarctica, *J. Geophys. Res.*, *98*, 22,553–22,568.
- Osborn, T., and W. Crawford (1980), *An Airfoil Probe for Measuring Turbulent Velocity Fluctuations in Water*, in *Air-Sea Interaction*, F. Dobson, L. Hasse, and R. Davis, pp. 369–386, Springer, New York.
- Paolo, F. S., H. A. Fricker, and L. Padman (2015), Volume loss from Antarctic ice shelves is accelerating, *Science*, *348*(6232), 327–331, doi:10.1126/science.aaa0940.
- Payne, A. J., A. Veli, A. P. Shepherd, D. J. Wingham, and E. Rignot (2004), Recent dramatic thinning of largest West Antarctic ice stream triggered by oceans, *Geophys. Res. Lett.*, *31*, L23401, doi:10.1029/2004GL021284.
- Pritchard, H. D., R. J. Arthern, D. G. Vaughan, and L. A. Edwards (2009), Extensive dynamic thinning on the margins of the Greenland and Antarctic ice sheets, *Nature*, *461*, 971–975.
- Rignot, E., S. Jacobs, J. Mouginot, and B. Scheuchl (2013), Ice-shelf melting around Antarctica, *Science*, *341*(6143), 266–270.
- Rignot, E., J. Mouginot, M. Morlighem, H. Seroussi, and B. Scheuchl (2014), Widespread, rapid grounding line retreat of Pine Island, Thwaites, Smith, and Kohler glaciers, West Antarctica, from 1992 to 2011, *Geophys. Res. Lett.*, *41*, 3502–3509, doi:10.1002/2014GL060140.
- Rudnick, D. L., et al. (2003), From tides to mixing along the Hawaiian Ridge, *Science*, *301*(5631), 355–357.
- Schoof, C. (2007), Ice sheet grounding line dynamics: Steady states, stability, and hysteresis, *J. Geophys. Res.*, *112*, F03S28, doi:10.1029/2006JF000664.
- Sheen, K. L., et al. (2014), Eddy-induced variability in southern ocean abyssal mixing on climatic timescales, *Nat. Geosci.*, *7*(8), 577–582.
- Shepherd, A., D. J. Wingham, J. A. D. Mansley, and H. F. J. Corr (2001), Inland thinning of Pine island glacier, West Antarctica, *Science*, *291*(5505), 862–864, doi:10.1126/science.291.5505.862.
- Shepherd, A., D. J. Wingham, and E. Rignot (2004), Warm ocean is eroding west Antarctic ice sheet, *Geophys. Res. Lett.*, *31*, L23402, doi:10.1029/2004GL021106.
- Soulsby, R. (1983), The bottom boundary layer of shelf seas, in *Physical Oceanography of Coastal and Shelf Seas*, vol. 35, edited by B. John, pp. 189–266, Elsevier Oceanogr. Ser., Elsevier.
- Stanton, T. P., W. J. Shaw, M. Truffer, H. F. J. Corr, L. E. Peters, K. L. Riverman, R. Bindschadler, D. M. Holland, and S. Anandakrishnan (2013), Channelized ice melting in the ocean boundary layer beneath Pine island glacier, Antarctica, *Science*, *341*, 1326–1329.
- Tennekes, H., and J. L. Lumley (1972), *A First Course in Turbulence*, MIT Press, Cambridge, Mass.
- Vaughan, D. G., H. F. J. Corr, R. A. Bindschadler, P. Dutrieux, G. H. Gudmundsson, A. Jenkins, T. Newman, P. Vornberger, and D. J. Wingham (2012), Subglacial melt channels and fracture in the floating part of Pine Island Glacier, Antarctica, *J. Geophys. Res.*, *117*, F03012, doi:10.1029/2012JF002360.
- Walker, D. P., M. A. Brandon, A. Jenkins, J. T. Allen, J. A. Dowdeswell, and J. Evans (2007), Oceanic heat transport onto the Amundsen Sea shelf through a submarine glacial trough, *Geophys. Res. Lett.*, *34*, L02602, doi:10.1029/2006GL028154.